Tribology Letters (2024) 72:51
https://doi.org/10.1007/s11249-024-01853-5

ORIGINAL PAPER

A Numerical Simulation of PFPE Lubricant Kinetics in HAMR Air Bearing

Roshan Mathew Tom[1] · Qilong Cheng[1] · David B. Bogy[1]

Received: 19 January 2024 / Accepted: 20 March 2024

Abstract
This report investigates the kinetics of lubricant molecules in the HAMR air bearing to understand the initiation and growth of PFPE contamination on the head surface. The collisions with the air bearing induce three forces—drag, thermophoresis, and lift. Of these, we find that lift forces are negligible. Then, a sensitivity analysis of the remaining two forces reveals the conditions where they dominate. Further, a hybrid simulation strategy is utilized to track their movements. The results show that the contaminations (smear) highly depend on the interplay between the thermophoresis and drag forces. We then explain the mechanism of the formation of the various observed patterns. Finally, we offer some recommendations to exploit the air bearing to contain smear on the head.

Keywords Heat-assisted magnetic recording (HAMR) · Air bearing · Lubricant · Smear

1 Introduction

Hard disk drives (HDD) are the leading technology for data center storage [1]. As the demand for data grows, the need to increase the storage density grows. In HDDs, a slider (head) writes data on a rotating disk. The sliding motion between the head and the disk forms a nano-tribological system where a thin layer of air and lubricant provide hydrodynamic lubrication to ensure consistent spacing and reliable operation. In conventional HDDs, read/write operations occur near room temperature. However, due to the superparamagnetic limit, increasing the density requires the use of materials with higher coercivity. However, it is not possible to write data in such materials at room temperature. Heat-Assisted Magnetic Recording (HAMR) overcomes this by embedding a laser in the head that heats a nanoscale spot on the recording disk to its curie temperature to write data [2]. However, the high temperature significantly impacts the lubricant layer, and contaminations start to accumulate on the head, which can lead to the head crashing on the disk. Therefore, controlling this contamination, called smear, remains an important technical challenge for the successful deployment of HAMR drives [3–5]. Figure 1 shows two AFM images of smear on a representative HAMR head.

The study of smear is challenging as the head–disk interface is multiscale and complex. It stretches hundreds of microns in the down-track and cross-track directions but only a few nanometers in the vertical direction. The presence of the TFC (Thermal fly-height control) heater and NFT (Near-field transducer) on the head raises the temperature above 700 K with temperature gradients exceeding 10^9 K/m. Further, the NFT forms a local protrusion [6] and induces electric field gradients exceeding 10^{16} V/m^2 [7]. The space between the head and the disk forms an air bearing of helium or air. The combination of these fields induces phenomena, such as thermal decomposition [8], thermophoresis, air shear [9], evaporation, condensation [10], and mechanical contact [3]. The disk is also composed of several materials, including Iron, Platinum, PFPE (perfluoropolyether) lubricants, and carbon overcoats [5]. Therefore, the contaminants can originate from a variety of sources by a variety of mechanisms. Numerical studies to understand these mechanisms take one of two approaches: a continuum mechanics-based approach [10–12] or a molecular dynamics (MD)-based approach [13, 14]. The former aims to model smear using bulk properties. It can reliably and quickly simulate smear patterns. However, since the head–disk spacing is often less than 10 nm, it does not account for the molecular effects. Further, it is cumbersome to characterize and couple the

✉ Roshan Mathew Tom
roshantom@berkeley.edu

[1] University of California at Berkeley, Berkeley, CA 94720, USA

Published online: 18 April 2024

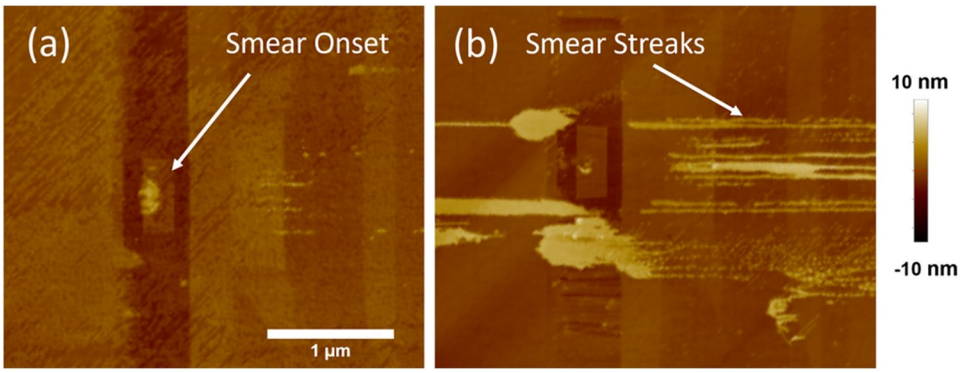

Fig. 1 AFM image of smear pattern on HAMR heads

properties from different fields, such as the electrical and thermal fields. The MD approach overcomes this problem by calculating the force on every molecule using an appropriate potential function. This ensures that all bulk and molecular phenomena are accounted for. Nonetheless, this process requires large computational power even to simulate up to a few nanoseconds. To our knowledge, none of these methods has yet replicated the streak-like features seen in Fig. 1b.

In this study, we are able to explain these streak-like features by focusing on the interaction between the air-bearing molecules to PFPE molecules. We employ a novel simulation methodology to simulate the kinetics of these molecules. First, we generate a force field using particle mechanics. This force represents the time-averaged force that a molecule experiences at a given point. Then, we track the trajectory of many lubricant molecules under the influence of this force field. Those that adsorb on the head are recorded and a density map is generated. This map can be visualized to see the growth of head lubricant over time. In section 2, we list the assumptions, derive the equations for the different forces arising from the air bearing, and present the simulation methodology. In section 3, we conduct simulations under various initial conditions and explain the mechanics of smear formation. Finally, in section 4, we apply the observations from the study to present some principles to control smear.

2 Numerical Model

We postulate that the air-bearing contribution to smear formation is a three-step process. The first step is the breaking of PFPE-to-surface bonds. In this case, they adhere to the disk by van der Waals (vdW) forces. The rise in the local temperature breaks this bond. The second step is the transport of PFPE molecules toward the head. This can be due to various factors, such as thermophoresis. The third step is lubricant condensation/adsorption, where the van der Waal's forces from the head capture these molecules to form smear in patterns as seen in Fig. 1.

2.1 Quantifying air-related forces

To quantify the air bearing-related forces experienced by a particle in the head–disk interface, we assume that they are composed of PFPE lubricants of varying lengths and thicknesses. The shape is approximated to be a cylinder defined by its length and radius. Helium-sealed drives are the industry standard for enterprise applications as they consume less power than corresponding air-filled drives [15]. Hence, the air bearing is assumed to be composed of helium atoms and, therefore, approximated as spheres. Although air contains negligible helium, we still use the term "air bearing" throughout the paper to maintain convention in this field. We also assume that the laser that heats the system has sufficient power to instantaneously bring the temperature of each particle to the local temperature.

Since the forces on a PFPE molecule arise due to collisions with the helium atoms, we begin by determining the velocity distribution of the helium atoms. Kinetic theory predicts that in a stationary container with uniform temperature, the velocity distribution of an ideal gas is given by the Maxwell–Boltzmann distribution. However, there are large velocity and temperature gradients in the head–disk spacing. The Chapman–Enskog (CE) distribution is able to account for these gradients. The first-order expansion of the CE distribution is given by [16]

$$f = f_0\left(1 - \frac{1}{n}\left(\frac{2k_BT}{m}\right)^{\frac{1}{2}}\boldsymbol{A}\cdot\boldsymbol{\nabla}(\ln T) - \frac{2}{n}\mathrm{B} : \boldsymbol{\nabla}\boldsymbol{v}_0\right) \quad . \quad (1)$$

Here, n, m, T, and $\boldsymbol{v}_o$ are the number density, mass, temperature, and mean molecular velocity of the helium atom, respectively. f_0 and k_B are the Maxwell–Boltzmann distribution and the Boltzmann constant, respectively. $\boldsymbol{A}$ and B are expansion terms. The CE distribution contains three terms. The first term is simply the Maxwell–Boltzmann distribution. The second and third terms are the correction terms to account for the temperature and velocity gradients,

respectively. Therefore, these three terms can give rise to three different forces in the head–disk spacing. In the literature, they are called the drag, thermophoresis, and Saffman lift forces. If κ and $\boldsymbol{v}$ are the thermal conductivity and molecular velocity of helium, the full expansion of these terms yields [16]:

$$f_0 = n\left(\frac{m}{2\pi k_B T}\right)^{3/2} \exp\left(-\frac{m(\boldsymbol{v})^2}{2k_B T}\right) \quad , \tag{2}$$

$$f_1 = f_0\left(-\frac{2m\kappa}{5nk_B^2 T}\left(\frac{m\boldsymbol{v}^2}{2k_B T} - \frac{5}{2}\right)\boldsymbol{v}\cdot\boldsymbol{\nabla}(\ln T)\right) \quad , \tag{3}$$

$$f_2 = f_0\left(-\frac{4m^2\kappa}{15nk_B^3 T^2}\left(\boldsymbol{v}^T\boldsymbol{v} - \frac{1}{3}\boldsymbol{v}^2\boldsymbol{I}\right) : \boldsymbol{\nabla}\boldsymbol{v}_0\right) \quad , \tag{4}$$

where f_0 corresponds to drag force, f_1 corresponds to thermophoresis, and f_2 corresponds to lift force. Further, the thermal conductivity of the gas can be calculated from the mass and diameter of the gas by [16]

$$\kappa = \frac{75}{64d_g^2}\sqrt{\frac{k_B^3 T}{\pi m}} \quad , \tag{5}$$

where d_g is the diameter of the gas particle. The next step in calculating the force is to define the PFPE–helium interactions. We assume that the helium atoms are chemically inert and undergo no adsorption to the PFPE molecule. In other words, the collision is purely specular. Then, the PFPE–helium interaction is modeled using a Lennard–Jones potential. For an n-alkane chain and helium, the potential function is given by [17]

$$U(r) = \epsilon\left[0.676\left(\frac{r - r_c}{\delta}\right)^{-11} - 1.031\left(\frac{r - r_c}{\delta}\right)^{-5}\right]. \tag{6}$$

Here, r is the distance center to center between the alkane chain and the helium atom and r_c is the radius of the alkane chain. The terms 0.676 and 1.031 are fitted from the general Lennard–Jones potential function summed from the individual atom–atom interactions. Further, $\epsilon = 3.404 \times 10^{-21}$ J and $\delta = 0.354$nm are appropriate Lennard–Jones parameters [17]. Due to the lack of literature about the interaction energy parameters of PFPE particles and considering the mutual cylindrical shape, we assume that the same potential function of n-alkanes applies to PFPE particles for this study.

Next, we calculate the momentum imparted by a helium atom to a PFPE molecule upon collision. By applying the principle of conservation of momentum, we assume that the net momentum gained by a PFPE molecule is the momentum lost by the helium atom. Since the collision is assumed to be specular, the change in momentum of the helium atom can be characterized by the scattering angle, χ, which is the angle by which the atom changes its direction upon collision. We assume that the length of the PFPE molecule is much greater than the radius of the helium atom, so there will be no deflection along the length of the cylinder. Therefore, we can reduce the system to a set of two circles—a thin slice of the PFPE molecule and the helium sphere. Then, the scattering angle is given by [18]

$$\chi(g, b) = \pi - 2\int_{r_{min}}^{\infty}\left[\frac{r^4}{b^2}\left(1 - \frac{2U(r)}{m_r g^2}\right) - r^2\right]^{-\frac{1}{2}} dr \quad , \tag{7}$$

where g is the in-plane relative velocity between helium and the PFPE molecule, m_r is the reduced mass of the helium-PFPE system, $U(r)$ is the helium-PFPE potential, and b is the impact parameter, which is the closest distance between the undisturbed trajectory of the helium and PFPE molecule. r_{min} is the distance of the closest approach, which is the largest root of the integrated of Eq 7. The reader can refer to Chapman (1991) [16] and Liu (2016) [18] for the detailed derivations. The net collision integral is given by

$$Q_{sp}(g) = L'\int_{-\infty}^{\infty}(1 - \cos\chi)db \quad , \tag{8}$$

where L' is the maximum distance beyond which the helium atom cannot collide with the PFPE molecule. Integrating $Q_{sp}(g)$ over the range of the velocities defined by the CE distribution, we calculate the three forces on a PFPE molecule as follows [18–20]:

$$F_{i,\perp} = m_r\int_{\boldsymbol{v}} f_i g g_\perp Q_{sp} d\boldsymbol{v},\ i = 0, 1, 2 \quad , \tag{9}$$

where the subscript $\perp$ refers to the component perpendicular to the axis of the PFPE molecule. The subscript i refers to the drag ($i = 0$), thermophoresis ($i = 1$), and lift ($i = 2$) forces. Since we made no assumption on the size and mass of the helium atom, Eq. 9 can be used for any spherical atom or molecule using an appropriate $U(r)$. Further, in addition to these forces, other effects such as optical forces [7] and ballistic jumps [21] can influence PFPE molecules. However, the conditions where they are significant, such as the presence of metallic nanoparticles or sub 4-nm spacing, are not present in this study. Hence, we focus only on the forces originating from the interaction between the helium atoms and PFPE molecules.

Table 1 Baseline values for sensitivity analysis

Parameter	Value
Mass of helium molecule (m)	6.6395×10^{-27} kg
Diameter of helium molecule (σ)	260 pm
Temperature, T	700 K
Air-bearing velocity (v_0)	15 m/s
Velocity gradient (∇v_0)	$\begin{bmatrix} 0 & 2 & 0 \\ 0 & 0 & 0 \\ 0 & 0 & 0 \end{bmatrix} \times 10^9/s$
Temperature gradient, ∇T	5×10^9 K/m
Length of PFPE molecule	5 nm
Radius of PFPE molecule	0.5 nm
PFPE monomer mass	91 amu
PFPE monomer length	350 pm

Table 2 Relative contribution of the three different forces

Type of force	Absolute Force	Relative Contribution
Drag force	1.76 pN	1
Thermophoretic Force	2.56 pN	1.46
Lift Force	1×10^{-10} pN	0

2.2 Sensitivity Analysis of Forces in the Head–Disk Interface

Next, we calculate and compare the magnitude of the three forces using the baseline values from Table 1. The results, tabulated in Table 2, show that the drag and thermophoretic force can be comparable, whereas the lift force is virtually zero. Therefore, we ignore the lift force for the remainder of this study.

Then, we conduct a sensitivity analysis of the relevant parameter space. Using the baseline values from Table 1, we individually vary each parameter for the thermophoresis and drag forces. The results are compared and analyzed to understand the conditions for which each force dominates in the head–disk interface. We start with the dimensions of the PFPE molecule—the radius and length. The radius primarily affects the potential function (Eq. 6), whereas the length is used to calculate the reduced mass for Eqs. 7 and 9. The comparisons are plotted in Fig. 2. In both cases, we see that there is a linear relationship between the force and the parameter for both thermophoresis and drag force. However, the thermophoresis force increases at a greater rate than the drag force. This indicates that for larger molecules, the thermophoresis force is more likely to be the dominating force.

Then, in order to study how the air-bearing composition affects these forces, we vary the properties of the gas. We considered the mass and the diameter of the gas molecule as the key parameters to investigate. The mass and diameter of the helium molecules is crucial in the Chapman–Enskog distribution (Eqs. 3–4). Further, the mass also influences the reduced mass in Eq. 7. The results are plotted in Fig. 3. By increasing the mass of the gas particle, the thermophoresis force remains approximately the same, whereas the drag force increases non-linearly. For the baseline case in Table 1, the drag force in heavier atoms is greater than in lighter atoms. Since the drag force aids in clearing the smear from the head, a gas medium with larger atoms/molecules appears to be more suitable for reducing smear. As a function of the molecular diameter, the drag force essentially remains the same, whereas the thermophoresis force decreases. This is because the diameter of the gas is only used in calculating the thermal conductivity (κ) which is relevant only for thermophoresis and lift force. Therefore, both graphs together show that the drag force tends to dominate for larger and heavier gas molecules, such as air. Meanwhile, for smaller

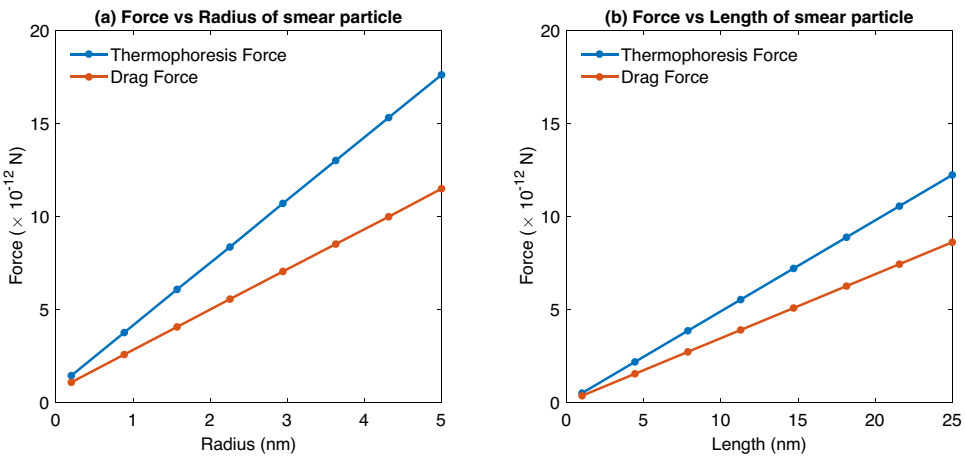

Fig. 2 Comparison of thermophoresis and drag force for various PFPE molecule parameters. **a** Variation with PFPE molecule radius keeping constant length of 5 nm. **b** Variation with PFPE molecule length keeping constant radius of 0.5 nm

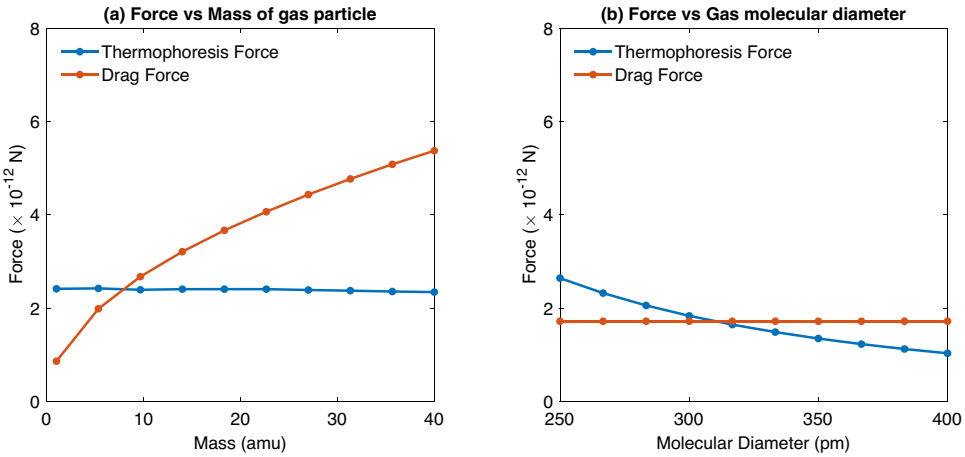

Fig. 3 Comparison of thermophoresis and drag force for various gas particle parameters. **a** Variation with the mass of the gas particle keeping a constant diameter of 260 pm and **b** variation with the diameter of the gas particle keeping a constant mass of 6.6395×10^{-27} kg

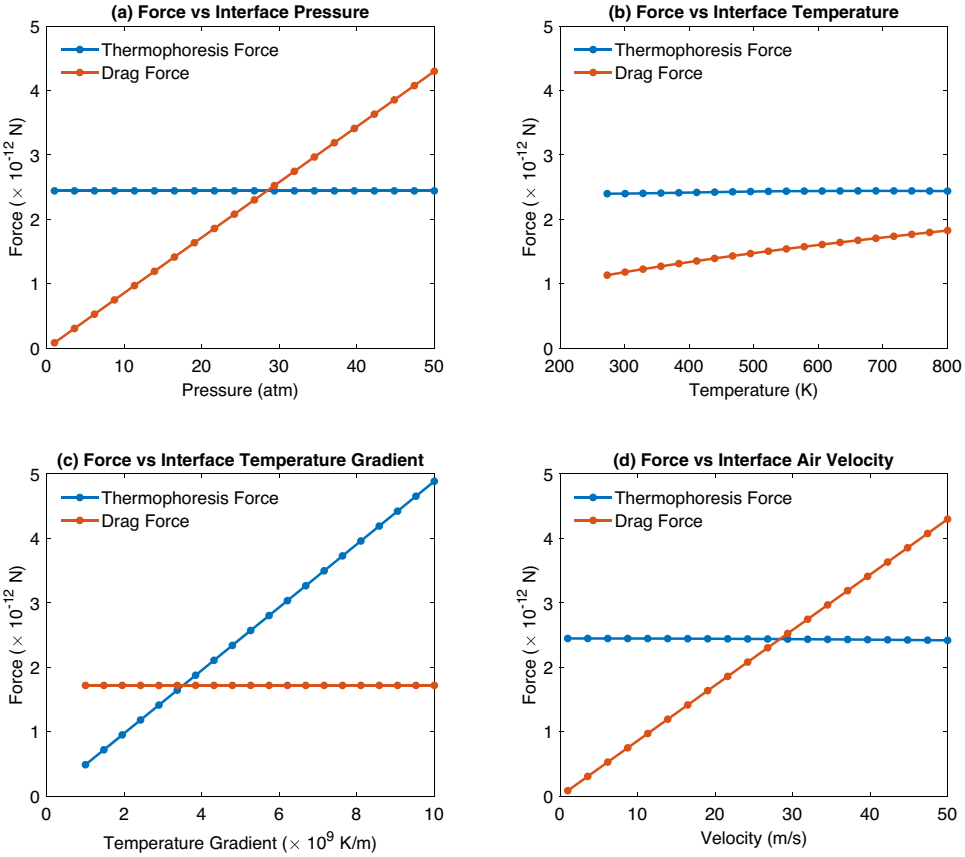

Fig. 4 Comparison of thermophoresis and drag force for various head–disk interface parameters. **a** Variation with the head–disk interface pressure, **b** variation with the head–disk temperature, **c** variation with the head–disk temperature gradient, and **d** variation with the velocity of the disk

and lighter particles, such as helium, the thermophoresis force tends to dominate.

Next, we consider the force dependence on the parameters in the head–disk interface. Four parameters are considered—the pressure, temperature, velocity of the disk, and temperature gradient. The results are plotted in Fig. 4. For the case of varying pressure (Fig. 4a), the thermophoresis force remains constant, whereas the drag force increases linearly. This indicates that in areas of low pressure, the thermophoretic force dominates. For the case of varying temperature (Fig. 4b), the thermophoresis force remains constant, whereas the drag force weakly increases with temperature. In the case of varying the temperature gradient (Fig. 4c), the drag force is constant, whereas the thermophoretic force increases linearly, which is expected since the temperature gradient drives thermophoresis. In the case of varying disk velocity (Fig. 4d), the drag force linearly increases, and the thermophoretic force remains

constant. This is also expected since the moving disk generates drag force on a PFPE molecule.

2.3 Smear Growth Simulation Methodology

Now that we can calculate the forces acting on a PFPE molecule, we can simulate smear growth on a HAMR head. We take a modified molecular dynamics approach [22]. The simulation box contains two plates. The top plate is stationary and represents a portion of the head. It has a dimension of 600 nm in the cross-track and down-track directions. The bottom plate moves at the velocity of 20 m/s in the down-track direction as it represents the disk. The dimensions of the bottom plate extend infinitely in both directions. However, the simulation is done only for locations directly below the head. This is possible because the forces are negligible at all other locations. The schematic of the resulting air bearing is shown in Fig. 5. Solving the transient heat conduction equation calculates the temperature profiles at the head and disk surfaces. The laser heating was represented as a circular heat source with a diameter of 10 nm, and the TFC heater was represented using joule heating of an element on the head. The head and the disk surface temperatures are shown in Fig. 6. The peak temperature at the disk is about 800 K due to the heating from the laser, whereas the head has a peak temperature of 500 K due to the losses from the NFT/WG and the TFC heating. At points near the center, the disk is hotter than the head. However, toward the edges, the head is hotter because the TFC heating occurs over a much larger area [3]. The temperatures at points between the disk and the head are linear interpolations between the corresponding points at the two ends. Thus, there is a temperature gradient in the vertical direction as well as in the in-plane directions. In the vertical direction, the force can be divided into two zones. First, near the NFT at distances < 200 nm from the hotspot, the thermophoretic force is directed from the disk to the head. Second, at locations far from the NFT, the thermophoretic force is directed toward the disk as the head is slightly hotter there than the disk. The former is the smear formation zone, and the latter is the smear removal zone. It is so named because, in the smear formation zone, the molecules tend to move toward the head, forming smear, whereas, in the smear removal zone, the molecules tend to detach from the head and fall back to the disk. Furthermore, in the in-plane direction, the temperature gradient causes the molecules to drift away from the hotspot center.

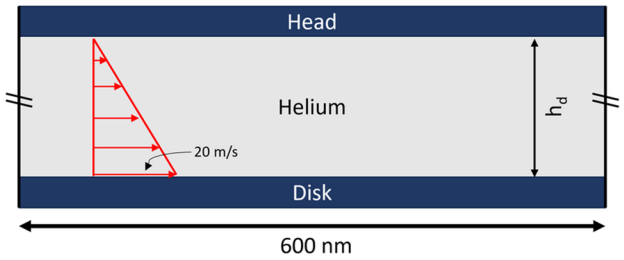

Fig. 5 A schematic of the simplified air bearing. It consists of flowing helium molecules at 20 atm pressure. Near the disk, the stream velocity is about 20 m/s, which then linearly tapers away to 0 m/s near the head. A reasonable assumption of the pitch is about 1×10^{-4} rad, which is less than 0.1-nm variation of spacing (h_d) over the length. Hence, we assume the air bearing to the uniform along the track

The dimensions of the lubricant molecules that form smear can vary depending on the number of monomer units, end groups, and whether it has undergone thermal decomposition. We can take Waltman's estimation for Tetraol-GT, which has a monomer weight of 91 amu and length of 345 pm [23] with a molecular weight of 1200 - 2200 amu [24]. Assuming the monomers lie flat, then the estimated length is between 4.5 nm and 8.3 nm. The physical lower limit for the diameter of a PFPE lubricant chain is $0.7 - 0.8$ nm [25]. However, the effective monolayer thickness is found to be up to 2 nm [24]. Therefore, the actual radius of a lubricant molecule can be anywhere between 0.35 nm and 1 nm. In order to simplify the simulation, we specify the lubricant

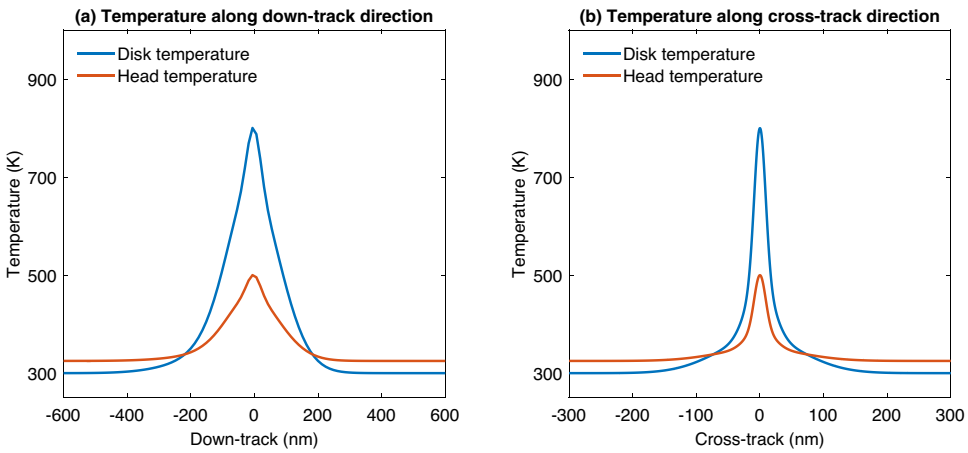

Fig. 6 Prescribed temperature for the first set of simulations. **a** Along the down-track direction; **b** along the cross-track direction

molecule to have a fixed length of 5 nm and a radius of 0.5 nm. The disk is then coated with a layer of these molecules.

Then, the van der Waals (vdW) interaction energy and the associated force between the lubricant molecule and the head or the disk are given by [26]:

$$E_{vdW} = \frac{A_{ham}}{12}\sqrt{\frac{r}{2d^3}}l \quad , \tag{10}$$

$$F_{vdw} = \frac{A_{ham}}{8}\sqrt{\frac{r}{2d^5}}l \quad , \tag{11}$$

where A_{Ham} is the Hamaker constant, r, l are the radius and length of the smear particle, and d is the distance between the center of the molecule and the surface. The Hamaker constant is approximated to be around 1×10^{-20} J, similar to Marchon and Saito [27]. The particles initially possess kinetic energies defined by the Maxwell–Boltzmann distribution. As the disk moves, the particles move to locations with different temperatures. We adjust the energy by a corresponding amount given by

$$E_{new} = E_{old} + \frac{3}{2}k_B\Delta T,$$

where ΔT is the temperature change. Therefore, we can define a particle's adsorption and desorption criteria by comparing its kinetic and vdW energy. If the vdW energy exceeds the kinetic energy, then the particle adsorbs, whereas if the kinetic energy exceeds the vdW energy, the particle desorbs.

The simulation starts with a layer of smear particles attached to the disk by vdW forces. The initial particle density of the smear particles on the disk is about 70000 particles/μm^2 or 25000 particles over the 600 nm $\times$ 600-nm disk inside the simulation box. As the simulation progresses in time, new portions of the disk enter the simulation domain, and new particles are created to fill it using the same particle density. If the disk has a velocity of 20 m/s, 840 particles are created every nanosecond At each time-step, the forces on each lubricant molecule are calculated, the adsorption/desorption criteria checked, and Newton's equation of motion determines the new position of each nanoparticle. Their orientation is assumed to be random. Finally, the molecules that adsorb on the head are recorded and a density map is used to visualize the smear pattern.

3 Results and Discussion

Our simulation consists of a clean helium-filled interface at a pressure of 2 MPa. The spacing varies from 4 to 35 nm. The total time of simulation is 3 μs with a 10-ps time-step (The trial runs showed that the choice of the time-step had little effect on the results). We simulate two diameters of laser heaters, 10 nm and 20 nm. To study the mechanics of its formation, we plotted the smear patterns of the head at two timestamps: 100 ns and 3000 ns. The former represents the smear onset phase, and the latter represents the smear growth phase.

The results for the smear onset phase are plotted in Fig. 7. In Fig. 7a and c, we see a bright spot in the center (Features A and D). This occurs because the lower spacing-to-hotspot ratio does not allow molecules to move around in the interface. The vertical thermophoretic force dominates and causes most particles to accumulate in the center. On the other hand, for Fig. 7b and d, we see multiple interesting features. Instead of having a centralized bright spot, there are two peaks with a slight offset from the center (Features B and G). Furthermore, in Fig. 7d, there is a streak in the cross-track direction (Feature E). These offsets arise because the spacing allows the in-plane thermophoretic force to separate the molecules from the center. In addition, we can also see two more spots farther away from the center (Features C and F). The trajectories that these particles take are more complicated. They arise from a delicate interplay between the thermophoretic and drag forces in different zones. After the molecule evaporates, it moves toward the head due to the vertical thermophoretic force. At the same time, since the molecule is upstream of the hotspot, the in-plane thermophoretic force pushes the molecule further upstream. As the molecule travels in this direction, it exits the smear formation zone and enters the smear removal zone. This effectively reverses the flow of the molecule, and it starts moving back to the disk. As it approaches the disk, it experiences the drag force and moves downstream. This causes the molecule to re-enter the smear formation zone and change its course toward the head. This time, the distance to the head is smaller, and the vertical thermophoretic force is sufficient to cause the molecule to reach the head. During this process, the molecule constantly faces an unhindered cross-track thermophoretic force. Since this process takes considerably longer, the molecule moves farther from the center, forming these additional spots. In our simulations, these additional dots were only observed for specific conditions. For the 10-nm hotspot, it was found to occur at a spacing between 8 to 10 nm. And for the 20-nm hotspot, it was found to be between 30 and 40 nm.

The results for the smear growth phase are plotted in Fig. 8. They show the evolution of the streak from the dots seen in Fig. 7. In the case of a lower spacing-to-hotspot ratio (Fig. 8a–c), there is only one thick streak. Other published experiments, such as that by Kiely et al. [3] and Xiong et al. [28], with smaller hotspot sizes and spacing show similar thick streaks. This qualitative similarity highlights the effectiveness of the simulation strategy in reproducing accurate patterns. Furthermore, in the case of a higher

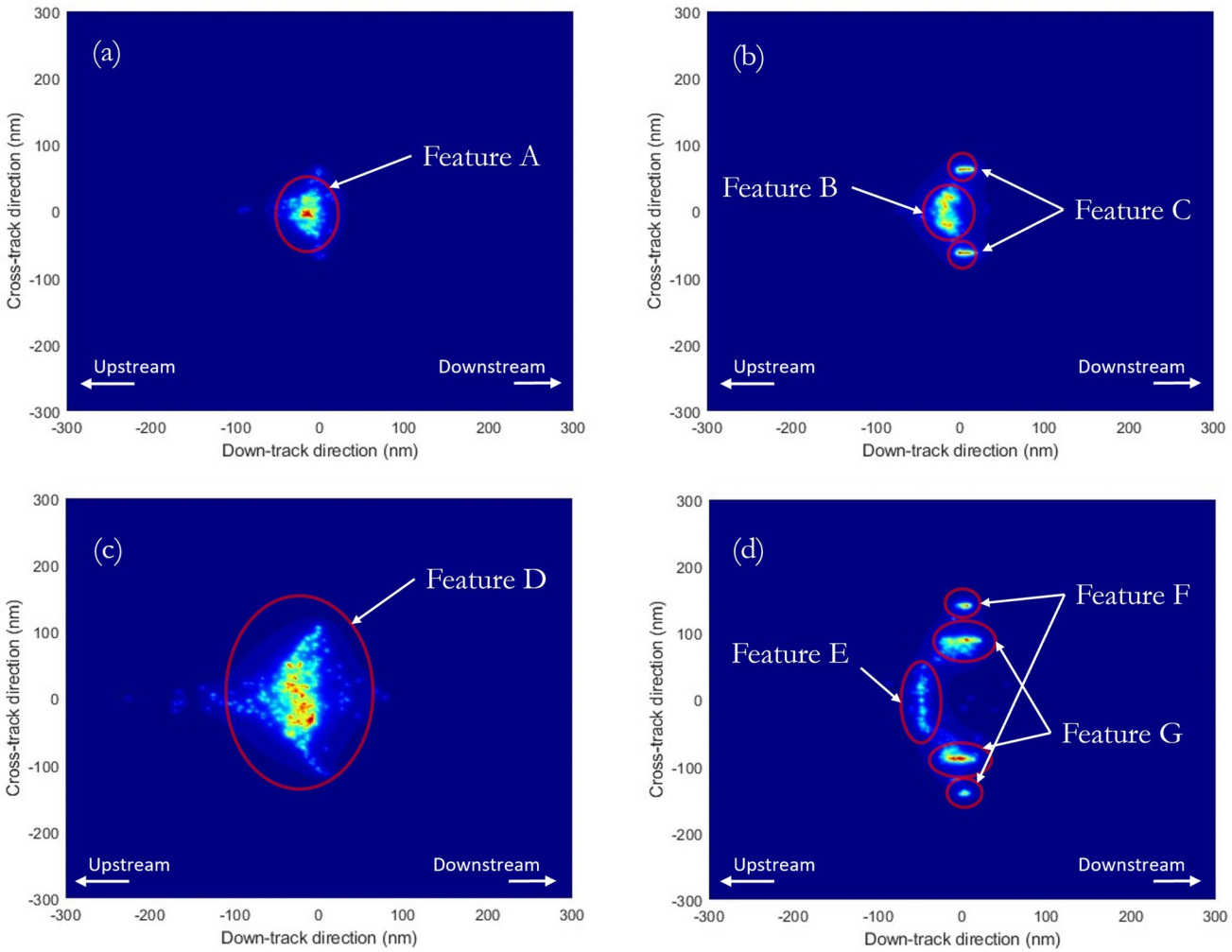

Fig. 7 Smear onset patterns for various parameters. **a** 10-nm hotspot and 4-nm spacing, **b** 10-nm hotspot and 10-nm spacing, **c** 20-nm hotspot and 10-nm spacing, and **d** 20-nm hotspot and 30-nm spacing

spacing-to-hotspot ratio (Fig. 8d), multiple streaks are observed. Near the center, it is filled with smear as in the other three cases. However, farther downstream, the streak diverges into two thick streams. They originate from the nanoparticles evaporating normally (Features B and G in Fig. 7). The thickness of these streaks for the larger hotspot is greater than those from the smaller hotspot since the area covered by the smear formation zone is greater if the hotspot is larger. Furthermore, Fig. 8b and d shows additional thinner streaks at the ends originating from the additional dots (Features C and F in Fig. 7). The length of these thinner streaks was also found to be much greater. The presence of multiple streaks with varying thicknesses is consistent with the results of the experiments from Fig. 1.

One important aspect to consider in the simulations is that we observe smear within a microsecond. However, in experiments, smear is observed only after a few seconds [29]. This disparity can be explained for two reasons. First, in the experiments, the smear volume measurements are taken after the disk and slider cool down. We know from simulations that the NFT temperature cools much slower than the disk [28]. Thus, it is possible that during this brief period, many of the particles loosely stuck to the head fall back to the disk. This means that the smear seen on an actual head is lower than the real-time smear in simulations. Also, in our evaporation criteria, we did not consider the bonding between the polar ends of the PFPE lubricant and the disk. We also did not consider the pressure caused by the helium molecules pressing down on the lube. These factors can reduce the evaporation rate and, subsequently, the smear volume.

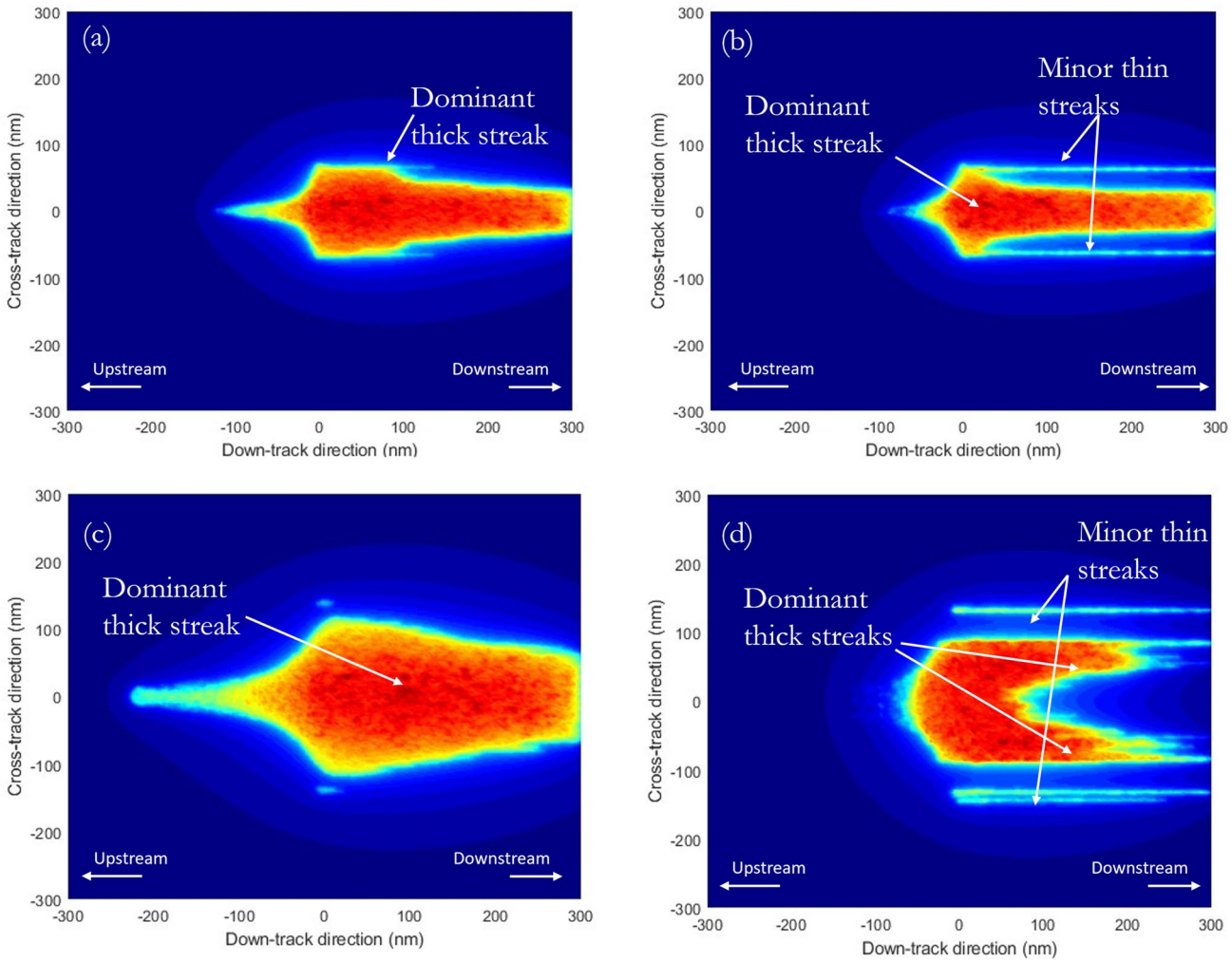

Fig. 8 Smear growth pattern for various parameters. **a** 10-nm hotspot and 4-nm spacing, **b** 10-nm hotspot and 10-nm spacing, **c** 20-nm hotspot and 10-nm spacing, and **d** 20-nm hotspot and 30-nm spacing

4 Conclusion

We know that in an actual head–disk interface, various parameters, such as pressure, temperature, and head–disk spacing, vary greatly at different locations. Since the sensitivity analysis and smear growth simulation show that these parameters are critical in determining the dominant force and growth characteristics, proper tuning can aid in controlling the growth of smear. Since thermophoresis grows faster than drag force with PFPE molecule dimensions, mechanisms such as thermal decomposition that break smear particles can help reduce smear buildup. Further, larger and heavier gas molecules show a net decrease in thermophoresis and an increase in drag force. Therefore, having such molecules can suppress smear buildup. Next, since pressure increases the drag force, designing the air-bearing surface (ABS) to give higher peak pressures in areas with higher susceptibility for smear will be helpful. Further, reducing the temperature gradient and increasing the speed of disk rotation can also reduce smear. Finally, from the smear simulation study, we notice that the smear streaks caused by the oscillations in temperature gradient are much thinner than central streaks. Therefore, designing such oscillations may be helpful. However, care must be taken to avoid other secondary effects from such oscillations.

Acknowledgements We want to thank Robert Smith, Sukumar Rajauria, and Qing Dai of Western Digital for their comments.

Author Contributions All authors contributed to the study's conception and design. Roshan Mathew Tom developed the methodology, conducted simulations, investigated the results, and wrote the first draft. Qilong Cheng conducted the experiments and reviewed the draft. David Bogy supervised the project. All authors read and approved the final manuscript.

Funding The work was supported by the Computer Mechanics Laboratory (CML) at the University of California, Berkeley.

Data Availability The data that support the findings of this study are available from the corresponding author upon reasonable request.

Declarations

Conflict of interest The authors have no relevant financial or non-financial interests to disclose

References

1. Armstrong, A.: Hard disk drives to remain dominant storage media in 2022. https://www.techtarget.com/searchstorage/feature/Hard-disk-drives-to-remain-dominant-storage-media (2022). Accessed 20 Nov 2023
2. Pan, L., Bogy, D.B.: Heat-assisted magnetic recording. Nat. Photonics **3**(4), 189–190 (2009). https://doi.org/10.1038/nphoton.2009.40
3. Kiely, J.D., Jones, P.M., Yang, Y., Brand, J.L., Anaya-Dufresne, M., Fletcher, P.C., Zavaliche, F., Toivola, Y., Duda, J.C., Johnson, M.T.: Write-induced head contamination in heat-assisted magnetic recording. IEEE Trans. Magn. **53**(2), 1–7 (2017). https://doi.org/10.1109/tmag.2016.2618842
4. Cheng, Q., Tom, R.M., Bogy, D.B.: Two strategies to mitigate thermally-induced material buildup in heat-assisted magnetic recording. Tribol. Lett. (2023). https://doi.org/10.1007/s11249-023-01723-6
5. Xiong, S., Smith, R., Schreck, E., Dai, Q.: Experimental study of material pick up on heat-assisted magnetic recording (HAMR) heads. Tribol. Lett. (2021). https://doi.org/10.1007/s11249-021-01455-5
6. Cheng, Q., Wang, H., Sakhalkar, S.V., Bogy, D.B.: Measurement of angstrom-level laser induced protrusion using touchdown in heat-assisted magnetic recording. Appl. Phys. Lett. **117**(15), 153105 (2020). https://doi.org/10.1063/5.0029051
7. Tom, R.M., Smith, R., Ruiz, O., Dai, Q., Bogy, D.B.: Optical forces in heat-assisted magnetic recording head-disk interface. Sci. Rep. (2023). https://doi.org/10.1038/s41598-023-35126-3
8. Yakata, K., Ichikawa, S., Tani, H., Lu, R., Koganezawa, S., Tagawa, N.: Smear and decomposition mechanism of magnetic disk PFPE lubricant film by laser heating in air and helium conditions. Tribol. Online **15**(3), 186–193 (2020). https://doi.org/10.2474/trol.15.186
9. Mendez, A.R., Bogy, D.B.: Lubricant flow and accumulation on the slider's air-bearing surface in a hard disk drive. Tribol. Lett. **53**(2), 469–476 (2013). https://doi.org/10.1007/s11249-013-0285-9
10. Sakhalkar, S.V., Bogy, D.B.: Viscoelastic lubricant deformation and disk-to-head transfer during heat-assisted magnetic recording. IEEE Trans. Magn. **55**(7), 1–6 (2019). https://doi.org/10.1109/TMAG.2018.2885434
11. Sakhalkar, S.V., Bogy, D.B.: Effect of rheology and slip on lubricant deformation and disk-to-head transfer during heat-assisted magnetic recording (HAMR). Tribol. Lett. (2018). https://doi.org/10.1007/s11249-018-1100-4
12. Smith, R., Rajauria, S., Brockie, R., Schreck, E., Dai, Q.: Opto-thermal simulation of metallic smear's impact on hamr technology. In: 2021 IEEE 32nd Magnetic Recording Conference (TMRC), pp. 1–2 (2021). https://doi.org/10.1109/TMRC53175.2021.9605106
13. Liu, Q., Huang, K., Zhu, X., Wang, G.: Study on the thermal decomposition of d-4oh PFPE lubricant by reactive molecular dynamic simulation for HAMR. IEEE Trans. Magn. **59**(3), 1–7 (2023). https://doi.org/10.1109/tmag.2022.3211698
14. Chen, X., Kawai, K., Zhang, H., Fukuzawa, K., Koga, N., Itoh, S., Azuma, N.: ReaxFF reactive molecular dynamics simulations of mechano-chemical decomposition of perfluoropolyether lubricants in heat-assisted magnetic recording. J. Phys. Chem. C **124**(41), 22496–22505 (2020). https://doi.org/10.1021/acs.jpcc.0c06486
15. Aoyagi, A., Stipe, B., Wood, R., Campbell, S., Che, X.: Helium sealed hard disk drive. J. Magn. Magn. Mater. **564**, 170146 (2022). https://doi.org/10.1016/j.jmmm.2022.170146
16. Chapman, S., Cowling, T.G.: Cambridge Mathematical Library: The Mathematical Theory of Non-uniform Gases. Cambridge University Press, Cambridge (1991)
17. Liu, C., McGivern, W.S., Manion, J.A., Wang, H.: Theory and experiment of binary diffusion coefficient of n-alkanes in dilute gases. J. Phys. Chem. A **120**(41), 8065–8074 (2016). https://doi.org/10.1021/acs.jpca.6b08261
18. Liu, C., Li, Z., Wang, H.: Drag force and transport property of a small cylinder in free molecule flow: a gas-kinetic theory analysis. Phys. Revi. E (2016). https://doi.org/10.1103/physreve.94.023102
19. Wang, J., Luo, S., Xia, G.: Thermophoretic force on nanocylinders in the free molecule regime. Phys. Rev. E (2017). https://doi.org/10.1103/physreve.95.033101
20. Luo, S., Wang, J., Yu, S., Xia, G., Li, Z.: Shear lift forces on nanocylinders in the free molecule regime. J. Fluid Mech. **846**, 392–410 (2018). https://doi.org/10.1017/jfm.2018.295
21. Tom, R.M., Bogy, D.B.: Ballistic material transport in hamr head-disk interface. In: 2023 IEEE 34th Magnetic Recording Conference (TMRC), pp. 1–2 (2023). https://doi.org/10.1109/TMRC59626.2023.10264026
22. Tom, R.M., Cheng, Q., Bogy, D.B.: A hybrid simulation for smear growth on hamr heads. In: 2023 IEEE International Magnetic Conference - Short Papers (INTERMAG Short Papers), pp. 1–2 (2023). https://doi.org/10.1109/INTERMAGShortPapers58606.2023.10228588
23. Waltman, R., Wiita, C.: Main chain effects in tetraol-functionalized perfluoropolyethers. Tribol. Online **10**(4), 262–272 (2015). https://doi.org/10.2474/trol.10.262
24. Waltman, R.J., Deng, H.: Low molecular weight z-tetraol boundary lubricant films in hard disk drives. Adv. Tribol. **2012**, 1–7 (2012). https://doi.org/10.1155/2012/964089
25. Tyndall, G.W., Leezenberg, P.B., Waltman, R.J., Castenada, J.: Interfacial interactions of perfluoropolyether lubricants with magnetic recording media. Tribol. Lett. **4**(2), 103–108 (1998). https://doi.org/10.1023/a:1019199004170
26. Israelachvili, J.N.: Chapter 13 - van der waals forces between particles and surfaces. In: Israelachvili, J.N. (ed.) Intermolecular and Surface Forces, 3rd edn., pp. 253–289. Academic Press, San Diego (2011). https://doi.org/10.1016/B978-0-12-375182-9.10013-2
27. Marchon, B., Saito, Y.: Lubricant thermodiffusion in heat assisted magnetic recording. IEEE Trans. Magn. **48**(11), 4471–4474 (2012). https://doi.org/10.1109/tmag.2012.2194138

28. Xiong, S., Wang, N., Smith, R., Li, D., Schreck, E., Dai, Q.: Material transfer inside head disk interface for heat assisted magnetic recording. Tribol. Lett. (2017). https://doi.org/10.1007/s11249-017-0860-6
29. Cheng, Q., Bogy, D.B.: Experimental study of smear formation and removal in heat-assisted magnetic recording. Tribol. Int. **165**, 107258 (2022). https://doi.org/10.1016/j.triboint.2021.107258